

Flat band physics in the charge-density wave state of $1T\text{-TaS}_2$

Amir Dalal,^{1,2} Jonathan Ruhman,^{1,2} and Jörn W. F. Venderbos^{3,4}

¹*Department of Physics, Bar-Ilan University, 52900, Ramat Gan, Israel*

²*Center for Quantum Entanglement Science and Technology, Bar-Ilan University, 52900, Ramat Gan Israel*

³*Department of Physics, Drexel University, Philadelphia, PA 19104, USA*

⁴*Department of Materials Science & Engineering,
Drexel University, Philadelphia, Pennsylvania 19104, USA*

(Dated: June 28, 2024)

$1T\text{-TaS}_2$ is the only insulating transition-metal dichalcogenide (TMD) with an odd number of electrons per unit cell. This insulating state is non-magnetic, making it a potential spin-liquid candidate. The unusual electronic behavior arises from a naturally occurring nearly flat mini-band, where the properties of the strongly correlated states are significantly influenced by the microscopic starting point, necessitating a detailed and careful investigation. We revisit the electronic band structure of $1T\text{-TaS}_2$, starting with the tight-binding model without CDW order. Symmetry dictates the nature of spin-orbit coupling (SOC), which, unlike in the 2H TMD structure, allows for strong off-diagonal “spin-flip” terms as well as Ising SOC. Incorporating the CDW phase, we construct a 78×78 tight-binding model to analyze the band structure as a function of various parameters. Our findings show that an isolated flat band is a robust feature of this model. Depending on parameters such as SOC strength and symmetry-allowed orbital splittings, the flat band can exhibit non-trivial topological classifications. These results have significant implications for the strongly correlated physics emerging from interacting electrons in the half-filled or doped flat band.

I. INTRODUCTION

Flat dispersion bands have the propensity to form a wide range of interaction-driven quantum phenomena. For this reason they are important to fundamental science as well as quantum technological applications [1]. Such bands may emerge due to interactions or strong orbital hybridization [2, 3]. The latter case has recently drawn a significant amount of interest due to the dominance of quantum geometrical effects [4]. Examples of interaction driven quantum phases resulting from flat bands include spin-liquid states, the fractional quantum Hall effect [5], fractional Chern insulators [6], unconventional superconductivity and various symmetry breaking states [7].

An interesting realization of a nearly flat band naturally occurs in the transition metal dichalcogenide (TMD) $1T\text{-TaS}_2$ [8]. At a temperature of $T \sim 200$ K this material undergoes a transition to a commensurate charge density wave (CDW) state, leading to a redistribution of the electronic charge and a large lattice distortion [9]. In this CDW state, clusters of 13 Ta atoms form a triangular lattice of stars-of-David (SoD), as shown in Fig. 3. Consequently, the band structure is dramatically reconstructed as a result of the CDW distortion, giving rise to the *spontaneous* formation of a nearly flat and half-filled band. Notably, the band is isolated from all other bands by gaps of the order of 100 meV.

At low temperature $1T\text{-TaS}_2$ is found to be a non-magnetic insulator. It is commonly accepted that the mechanism behind the insulating behavior is Mott physics driven by Coulomb repulsion [10]. No sign of magnetic ordering has been detected down to lowest cryogenic temperatures [11], which makes this system a natural spin-liquid candidate [12]. Support for possible spin

liquid physics was offered by STM experiments on thin layers of $1T\text{-TaSe}_2$ [13], which found incommensurate peaks in the quasi-particle interference patterns consistent with a spinon Fermi surface (SFS). However, theoretical and experimental studies propose that the bulk insulating behavior stems from interlayer dimerization (see for example Ref. [14]).

From the theoretical perspective, efforts to understand the intriguing electronic and magnetic properties observed in $1T\text{-TaS}_2$ have focused on two separate but related aspects of the problem. The first concerns the electronic properties of the flat band [8]. First-principles electronic structure calculations suggested that spin-orbit coupling is crucial for the formation of the flat band [15], but more recent work has shown that an isolated flat band can emerge even when spin-orbit coupling is ignored [16, 17]. In particular, a recent study revealed that an insightful tight-binding description of the relevant Ta-derived bands can be obtained by choosing an orbital basis tied to the local near-octahedral environment of the TaS_6 clusters [18]. In this basis, in which the active bands are formed from t_{2g} states, the band dispersion obtained from first-principles calculations can be approximated by restricting to intra-orbital hopping, which provides a useful idealized limit for understanding the emergence and structure of the flat band.

While the electronic structure of the flat band is generally addressed within single-particle band theory, either through first-principles calculations or effective Hamiltonian modeling, gaining insight into the observed nonmagnetic insulator at low temperatures requires including electron correlations. This aspect of the problem (i.e., the Mott physics) has therefore been addressed within the framework of an effective multi-orbital Hubbard model—a common approach in the realm of strongly correlated

electron materials [12]. Based on this description an XXZ spin Hamiltonian has been proposed, based on which the magnetic ordering and spin liquid phenomena can be studied [19].

The construction of an effective Hubbard model and resulting low-energy spin-spin model relies on an appropriate microscopic starting point. In the case of 1T-TaS₂, this means obtaining an accurate model for the flat band, from which a suitable spin model can then be derived. With this motivation in mind, we construct a microscopic tight-binding model for 1T-TaS₂ and revisit the precise nature of the flat band in 1T-TaS₂. We do so by approaching the band reconstruction in the CDW state and the resulting emergence of an isolated flat band from a different perspective compared to previous work. In our approach the CDW state is viewed as a superlattice of weakly coupled SoD clusters, such that the mini-bandstructure in the CDW state can be interpreted as a collection of nearly flat dispersive bands derived from the energy levels of the individual clusters. Viewed in this light, the nature of the flat band can be traced back to the molecular orbitals of the SoD clusters, which we systematically construct. We will show that this gives important insight into the flat band physics and leads to a unified understanding of previous descriptions of the band reconstructions. We highlight in particular the role played by spin-orbit coupling.

Exploiting the paradigm of weakly coupled clusters, we examine and discuss three possible flat band scenarios, which are sharply distinguished by the symmetry and structure of the cluster levels. The realization of these scenarios depends on the relative strength of parameters of the model which affect the ordering of energy levels of a single SoD cluster, such as crystal field splitting, hopping, and spin-orbit coupling. We show that it is possible, at least in principle, to achieve a level crossing of cluster states with opposite parity, which can give rise to topological minibands once the clusters are coupled to form a superlattice.

Our analysis of the CDW state as coupled clusters thus provides a unifying framework for addressing the single-particle flat band physics of 1T-TaS₂ and also lays the foundation for microscopically grounded descriptions of the Mott state.

II. TIGHT BINDING MODEL FOR 1T-TAS₂

We begin by introducing a microscopic tight-binding model for 1T-TaS₂. We proceed in three steps. First, we consider a tight-binding model for an undistorted 1T-TaS₂ monolayer without spin-orbit coupling, which serves as the root model for the next steps. We then include the effect of spin-orbit coupling and comment on the differences with the 1H D_{3h} TMDs. In the final step, we include the effects of the CDW by periodically alternating the parameters in the tight-binding model.

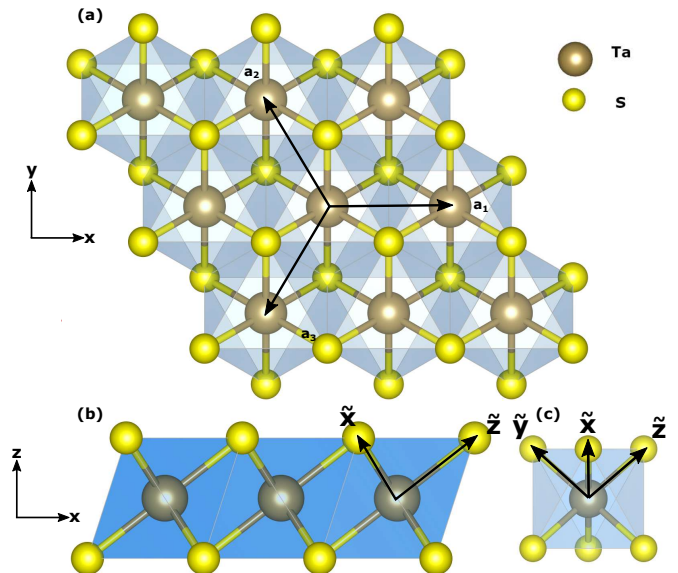


FIG. 1. The crystal structure of 1T-TaS₂. Top and side views are shown in panels (a),(b) respectively. A single octahedron with the corresponding aligned axes is shown in panel (c).

A. Tight-binding model in the absence of SOC and the CDW

The crystal structure of a 1T-TaS₂ monolayer is shown in Fig. 1. The tantalum atoms form a triangular lattice that sits between two triangular lattices of sulfur atoms. Importantly, the top and bottom triangular sulfur layers are shifted, such that each Ta atom is surrounded by six S atoms forming a trigonally distorted octahedron (see panels b and c of Fig. 1). The resulting structure has trigonal D_{3d} point group symmetry, generated by the threefold rotation C_{3z} , the twofold rotation C_{2x} , and the inversion \mathcal{I} .

The atomic orbitals relevant for the electronic structure predominantly belong to the 5d multiplet. To understand the effect of crystal field splittings on the 5d states it is instructive to consider the (distorted) octahedral environment of the Ta atoms. If the distortion away from perfect octahedral coordination is neglected, then the locally cubic environment splits the d states into a t_{2g} and an e_g multiplet. The three t_{2g} states ($d_{\tilde{y}\tilde{z}}$, $d_{\tilde{z}\tilde{x}}$, $d_{\tilde{x}\tilde{y}}$) are lower in energy and constitute the relevant valence electron manifold. To denote the t_{2g} states here we have used a coordinate system $(\tilde{x}, \tilde{y}, \tilde{z})$ aligned with the octahedron, which is rotated with respect to the crystallographic coordinate system (x, y, z) , as shown in Fig. 1(b) and (c). The usefulness of a description in terms of the octahedral coordinate system was pointed out in Ref. 18, which showed in particular that such description provides a basis for considering insightful idealized limiting cases (e.g., neglecting interorbital hopping).

The crystal field generated by the trigonal distortion of the octahedra splits the t_{2g} states further into a sin-

gle non-degenerate level and a degenerate doublet. In the crystallographic coordinate system, which is the natural choice when distortions are properly accounted for, these states are given by d_{z^2} and $(d_{x^2-y^2}, d_{xy})$ (with a symmetry-allowed admixture of d_{xz} and d_{yz}). These states transform as the A_{1g} and E_g representations of the D_{3d} point group. To capture the electronic properties of $1T$ -TaS₂ close to the Fermi energy, we consider a tight-binding model for these three orbitals. We choose a basis of states given by $\{|d_+\rangle, |d_0\rangle, |d_-\rangle\}$, where $d_0 \equiv d_{z^2}$ and $d_{\pm} \equiv id_{x^2-y^2} \pm d_{xy}$. (We emphasize that the d_{\pm} states also have support on $d_{xz} \pm id_{yz}$, see Appendix A.) In the chosen basis, the tight-binding Hamiltonian takes the form

$$H_0(\mathbf{k}) = \begin{pmatrix} \varepsilon_1 + t_2\gamma_{\mathbf{k}} & t_3\lambda_{\mathbf{k}} & t_4\lambda_{\mathbf{k}}^* \\ c.c & \varepsilon_0 + t_1\gamma_{\mathbf{k}} & t_3\lambda_{\mathbf{k}} \\ c.c & c.c & \varepsilon_1 + t_2\gamma_{\mathbf{k}} \end{pmatrix}, \quad (1)$$

where we have included all symmetry-allowed couplings up to nearest neighbor hopping. In particular, here $\varepsilon_{0,1}$ are the on-site energies of the d_0 and d_{\pm} states, such that the crystal field splitting is $\Delta = \varepsilon_1 - \varepsilon_0$, and $t_{1,2}$ are the intra-orbital nearest neighbor hopping amplitudes. The interorbital hopping amplitudes are given by t_3 and t_4 , and the functions $\gamma_{\mathbf{k}}$ and $\lambda_{\mathbf{k}}$ are defined as

$$\gamma_{\mathbf{k}} = c_1 + c_2 + c_3, \quad \lambda_{\mathbf{k}} = c_1 + \omega c_2 + \omega^2 c_3, \quad (2)$$

where $c_i \equiv \cos(\mathbf{k} \cdot \mathbf{a}_i)$ and $\omega \equiv e^{i2\pi/3}$. Here \mathbf{a}_i are the primitive lattice vectors $\mathbf{a}_i = \cos\phi_i\hat{x} + \sin\phi_i\hat{y}$ with $\phi_i = 2\pi(i-1)/3$.

The values of t_1, \dots, t_4 , ε_0 and ε_1 , which obtain the best fit with DFT calculations [15] are listed in Table. I. The resulting bands and their comparison to DFT are presented in Fig. 2.(a).

B. Spin-Orbit Coupling

The next step is to include the effect of spin-orbit coupling (SOC). The form of the spin-orbit interaction depends in a crucial way on the nature of the orbitals involved, in particular the nature of the $|d_{\pm}\rangle$ states, as we will explain below [20, 21]. In the case of $1T$ -TaS₂ the appropriate form of the spin-orbit coupling Hamiltonian is given by

$$H_{\text{SO}} = \lambda_0 \cos\theta L_z \sigma_z + \lambda_0 \sin\theta (L_x \sigma_x + L_y \sigma_y), \quad (3)$$

where $(\sigma_x, \sigma_y, \sigma_z)$ are the three spin Pauli matrices and (L_x, L_y, L_z) are spin angular momentum matrices in the space of d -orbitals. Here we have introduced an overall energy scale associated with spin-orbit coupling, given by λ_0 , and an angle θ , which determines the relative weight of the spin-preserving Ising and spin-flip terms. As such, θ interpolates between the Ising limit ($\theta = 0$) and the isotropic limit ($\theta = \pi/4$).

Many previous studies of TMD materials have considered electronic models that only include the Ising

spin-orbit coupling. This is appropriate for the $1H$ materials with D_{3h} symmetry, since in these systems the $(d_{x^2-y^2}, d_{xy})$ orbitals are symmetry-distinct from the (d_{xz}, d_{yz}) orbitals, forbidding these states to mix. Projecting the atomic spin-orbit coupling of the $L = 2$ d -states with a $S = 1/2$ spin into the subspace of the $(d_{x^2-y^2}, d_{xy})$ and d_z^2 orbitals (i.e., the relevant valence and conduction states), yields the Ising term only; the spin-flip terms vanish. This is markedly different in the $1T$ structures, where the $(d_{x^2-y^2}, d_{xy})$ and (d_{xz}, d_{yz}) orbitals can mix, forming the d_{\pm} doublet introduced above. Due to the admixture of (d_{xz}, d_{yz}) the spin-flips do not strictly vanish, giving rise to the more general form (3). The angle θ is therefore related to the orbital content of the d_{\pm} states. More details are provided in Appendices A and C.

In the specific context of $1T$ -TaS₂ only the Ising spin-orbit coupling was previously considered [19, 20]. Its effect on the electronic states is to split the orbital doublet $|d_{\pm}\rangle$ into two Kramers doublets, which constitutes one possible scenario for realizing a single twofold Kramers degenerate flat band in the CDW state. We return to this point in Sec. III when we discuss the nature of the flat band. There are two compelling reasons to consider the more general form of the spin-orbit coupling Hamiltonian given by (3). First, including only the Ising term leaves an unphysical continuous spin rotation symmetry around the z axis, which, for instance, has consequences for the form of the effective low-energy spin Hamiltonian derived from the microscopic multi-orbital model once interactions are included. We briefly discuss this in Sec. V. Second, the more general form gives access to the isotropic limit, given by $\theta = \pi/4$, which is useful for gaining insight into electronic structure of $1T$ -TaS₂. The isotropic limit corresponds to perfect octahedral coordination of the S atoms, in which case spin-orbit coupling can simply be understood as arising from three degenerate t_{2g} states $(d_{\tilde{y}\tilde{z}}, d_{\tilde{z}\tilde{x}}, d_{\tilde{x}\tilde{y}})$ in the octahedral coordinate frame (see Appendices C). When the trigonal distortion is weak, which is a valid assumption in $1T$ -TaS₂, the isotropic limit is expected to provide a good approximation to the value of θ .

C. The Charge-Density Wave

$1T$ -TaS₂ undergoes a sequence of phase transitions upon lowering the temperature [9, 22]. First, at roughly $T = 360$ K it undergoes an incommensurate CDW transition into a reconstructed metallic state. Subsequently, around $T = 200$ K, a lock-in transition occurs at which the CDW becomes commensurate. This second transition is strongly first order with hysteresis [23].

In what follows, we will only be interested in the low temperature commensurate CDW phase. In this commensurate state the crystal is reconstructed and forms a $\sqrt{13} \times \sqrt{13}$ superlattice composed of stars-of-David clusters, as shown in Fig. 3. Each start-of-David (SoD)

TABLE I. List of parameters used in the tight binding model, with and without CDW

Lattice parameters	Value	Units	Description	Reference
a	3.36	Å	Lattice constant	Ref. [9]
ω	$e^{i2\pi/3}$	-	Trigonal phase factor	
ε_0	1.48	eV	On-site energy of d_0 orbital	Fitted to DFT[15]
ε_1	1.34	eV	On-site energy of d_{\pm} orbitals	Fitted to DFT[15]
t_0	-0.1	eV	d_0 - d_0 hopping parameter	Fitted to DFT[15]
t_1	-0.15	eV	d_{\pm} - d_{\pm} hopping parameter	Fitted to DFT[15]
t_3	-0.28	eV	d_0 - d_{\pm} hopping parameter	Fitted to DFT[15]
t_4	0.43	eV	d_{\pm} - d_{\mp} hopping parameter	Fitted to DFT[15]
λ_0	0.640	eV	SOC strength	Phenomenological Parameter (value is best fit to Ref.[15])
θ	-	-	Relative strength of spin-flip and spin conserving SOC terms ($\theta = 0$ is the Ising limit and $\theta = \pi/4$ is the isotropic limit)	Phenomenological Parameter
<hr/>				
CDW parameters				
s_{β}	0.064	-	Contraction parameter for β ring Eq. (6)	Fitted to DFT[15]
s_{γ}	0.043	-	Contraction parameter for γ ring Eq. (6)	Fitted to DFT[15]
ξ	1.4	Å	Wannier orbital width	Fitted to DFT[15]
Δ	$\varepsilon_1 - \varepsilon_0$	eV	Orbital bias	Phenomenological Parameter

consists of 13 Ta atoms, with one central atom and two shells of 6 nearest neighbours (inner shell) and 6 next-to-nearest neighbours (outer shell). These two shells contract radially towards a central Ta atom (see Fig. 3). Consequently, each SoD forms a 13 atoms unit cell in a new triangular superlattice. The electronic states close to the Fermi energy are dramatically affected by this distortion and exhibit insulating behavior at low temperature, which is believed to be a Mott insulator.

It is important to note that the commensurate CDW phase spontaneously breaks the C_{2x} symmetry, giving rise to two distinct tiling patterns. The sample may be a unidomain or multidomain, in which case domain walls will appear (see STM data presented in Ref. [24]). Other types of domain walls are also possible, which correspond to fractional dislocations of the superlattice [25]. Recently, voltage driven switching between the two tiling configurations was demonstrated in Ref. [26]. However, in what follows, we choose a particular tiling pattern and assume the sample is a unidomain and leave the exploration of these intriguing domain walls to future work. The primitive superlattice vectors are chosen as $\mathbf{L}_1 = 3\mathbf{a}_1 + 4\mathbf{a}_2$ and $\mathbf{L}_2 = -\mathbf{a}_1 + 3\mathbf{a}_2$. Notice that the axes of the primitive vectors is rotated with respect to the original one $\{\mathbf{a}_1, \mathbf{a}_2, \mathbf{a}_3\}$ by $\approx 13.9^\circ$.

To incorporate the effects of the CDW we promote the tight-binding model to a superlattice model by increasing the unit cell, which introduces an additional intra-super cell degree of freedom corresponding to the site number. In accordance with the literature we distinguish three types of sites, denoted α, β, γ (see Fig. 3), where β_n and γ_n with $n = 0, \dots, 5$ label the sites in the α and β shells. The basis states of the tight tight-binding model are then $|\alpha, d_{0,\pm}\rangle$, $|\beta_n, d_{0,\pm}\rangle$, and $|\gamma_n, d_{0,\pm}\rangle$. As a result of the

radial contraction, the position of the β and γ sites in the unit cell is modified and takes the form

$$\mathbf{r}_{\beta,\gamma} = \mathbf{r}_{0,\beta,\gamma}(1 - s_{\beta,\gamma}) \quad (4)$$

where \mathbf{r}_0 is the position before the contraction and the two dimensionless parameters $s_{\beta,\gamma}$ account for the displacement in the CDW state. The values of the displacement are taken from X-ray scattering experiments [27] and DFT [15] (see Table I).

We now discuss how the superlattice tight-binding model is lifted from the model for undistorted 1T-TaS₂ introduced above. Three aspects warrant discussion: the on-site couplings (i.e. crystal fields, spin-orbit coupling), the hopping within a cluster, and the hoppings between clusters. We keep the form of the on-site terms the same as before, which is to say that we neglect small deviations within the supercell¹. Hence, the on site couplings remain $\varepsilon_{0,1}$ and (λ_0, θ) . However, we treat $\Delta \equiv \varepsilon_1 - \varepsilon_0$ as a parameter and explore the dependence of the mini-band electronic structure on the value of the crystal field splitting.

Next, we turn to the hopping terms, which are modified due to the change in the overlap between neighboring Wannier orbitals of the undistorted lattice. We divide our hopping terms into intra- and inter-unit-cell hopping terms, denoted by H_{ij}^{intra} , H_{ij}^{inter} . We choose the gauge²

¹ In principle, this potential also depends on the shell α, β and γ . However, the dependence on shell introduces four additional fitting parameters, which have very little influence on the resulting band-structure and Bloch wave functions. Thus, to prevent over parameterization we omit this dependency.

² We exploit individual gauge freedom of each site to absorb the

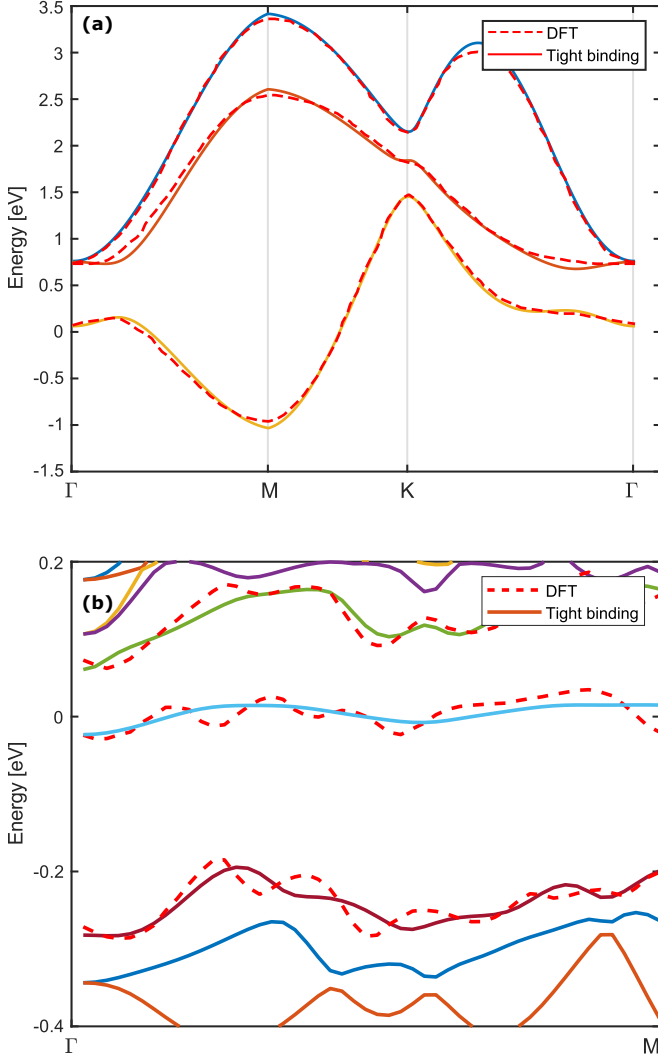


FIG. 2. Fit of the tight binding parameters to the DFT result [15]. (a). The dispersion of 1T-TaS₂ without CDW effects. Obtained by diagonalizing the Hamiltonian $H = H_0 + H_{SOC}(L_2, \theta = 0)$ and fit to DFT data. (b). The dispersion of 1T-TaS₂ in the CDW phase. Obtained by diagonalizing Eq (7). In both figures, the solid lines are the bands obtained from the best fit corresponding to the parameters in Table I. The dashed lines are the bands from the DFT data.

such that the intra-unit-cell hopping Hamiltonian is k independent and the inter-unit-cell hopping Hamiltonian come with the k dependent phases $e^{i\mathbf{L}_{ij}\cdot\mathbf{k}}$, where \mathbf{L}_{ij} are the lattice vectors connecting lattice sites i and j . Under these conditions, the lowest order correction to the hopping can be written as follows

$$\begin{aligned} H_{ij}^{intra} &= S_{ij}\hat{T} \\ H_{ij}^{inter}(\mathbf{k}) &= S_{ij}e^{i\mathbf{L}_{ij}\cdot\mathbf{k}}\hat{T} \end{aligned} \quad (5)$$

phase factor associated with their displacement with respect to the central α atom.

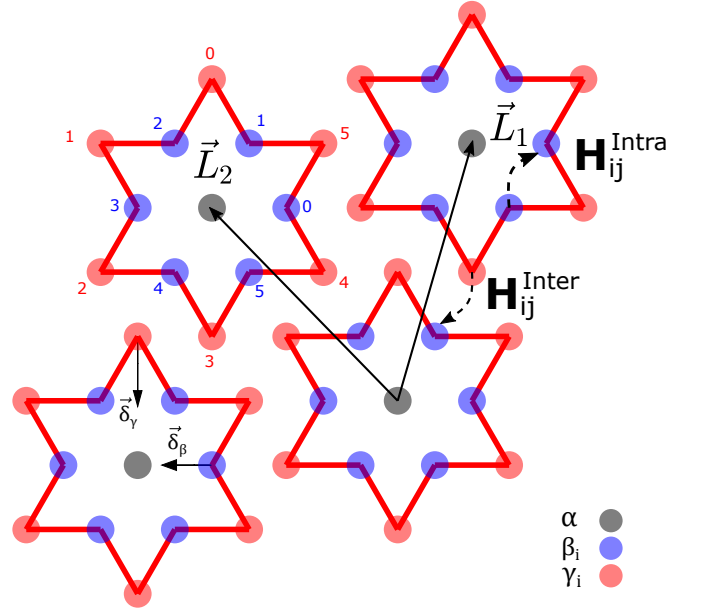


FIG. 3. The superlattice structure in the CDW phase. The central atom is denoted by α (grey), the inner shell is denoted by β_i (blue) and the outer shell is denoted by γ_i (red). Each atom on the inner (outer) shell contracts radially with contraction vector δ_β (δ_γ). The vectors \mathbf{L}_1 and \mathbf{L}_2 denote the CDW lattice vectors. H_{ij}^{Intra} and H_{ij}^{Inter} denote the hopping matrix elements inside and between CDW sites, respectively.

where \hat{T} is the appropriate hopping matrix along the direction of the ij -bond (see Appendix B for more details). Notice we have introduced a correction to the hopping amplitude encapsulated in the matrix

$$S_{ij} \approx 1 + (s_i - s_j)r_{ij}^2/\xi^2. \quad (6)$$

Here ξ is the length scale of the Wannier orbital on each site, which we will treat as a phenomenological parameter.

The resulting tight-binding Hamiltonian is a 78×78 matrix (2 spins \times 3 orbitals \times 13 sites) given by

$$H_{ij}^{CDW}(\mathbf{k}) = [H_{ii}\delta_{ij} + H_{i,j}^{intra} + H_{i,j}^{inter}(\mathbf{k})]. \quad (7)$$

We note that the model above includes two phenomenological parameters; the orbitally selective energy shift, Δ , and the extent of the Wannier orbitals, ξ . To determine the values of these parameters we fit the resulting flat band and its two nearest neighboring bands to DFT calculations [15]. The results of an unbiased fitting procedure are presented in Fig. 2.b and yield $\xi = 1.4\text{\AA}$ and $\Delta = 0.55\text{ eV}$.

III. THE CHARGE-DENSITY WAVE STATE VIEWED AS A LATTICE OF WEAKLY COUPLED CLUSTERS

In this section we turn to one of the central results of this paper: an analysis of the flat band electronic

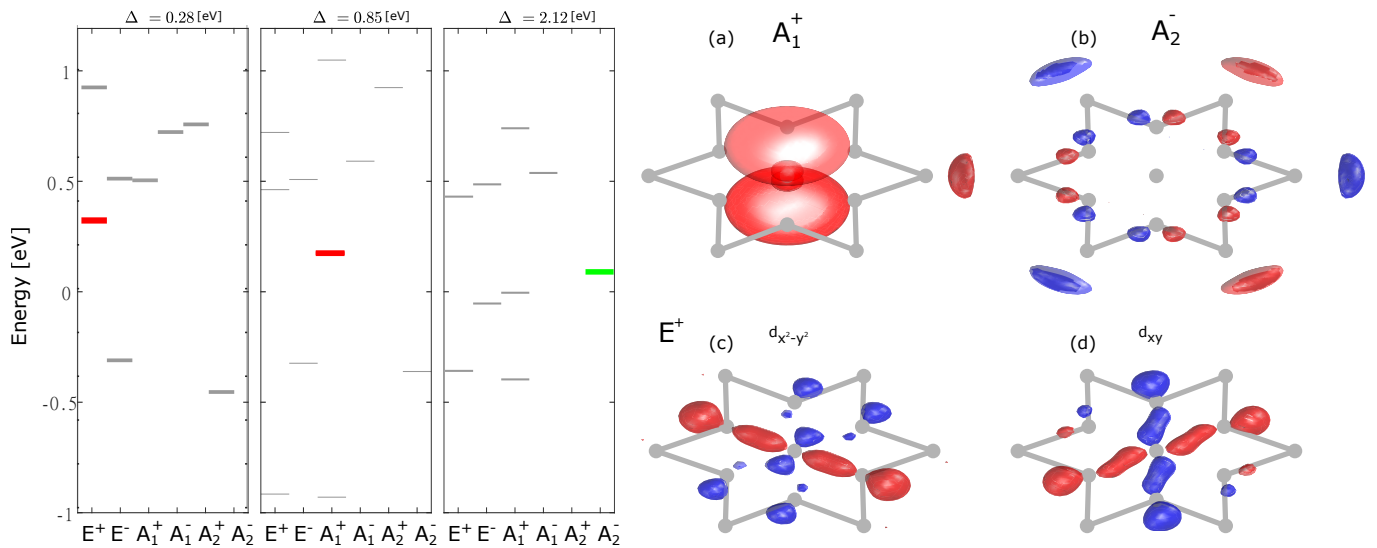


FIG. 4. (a) to (c) The energy spectrum of the molecular orbital, for fixed SOC strength $\lambda_0 = 0$ different values of Δ [(a) corresponds to $\Delta = 0.28$ eV, (b) corresponds to $\Delta = 0.85$ eV and (c) corresponds to $\Delta = 2.12$ eV]. The state corresponding to seventh band is colored red or green corresponding to whether the cluster state is even or odd under inversion, respectively. (d) to (f) The real space wave-function for each the states indicated in panels (a) to (c) with the corresponding symmetry label. The color indicates sign of the wave function, and the grey lines represent the SoD cluster.

structure in terms of weakly coupled SoD clusters. The starting point for this analysis are the isolated clusters (i.e., the basic units of the CDW superlattice), for which we systematically construct symmetrized cluster states. These symmetrized cluster states can be understood as the molecular orbitals of the 13-site units. When expressed in a basis of molecular orbitals, the Hamiltonian of a single SoD cluster is block diagonal and its energy levels can be labeled by the symmetry quantum numbers of the symmetrized states. The symmetry-resolved spectrum of energy levels of a single cluster then allows us to identify the state which forms the flat band, thus providing important insight into the nature of the flat band and its dependence on the parameters of the cluster Hamiltonian.

In constructing the symmetrized cluster states we proceed in two steps. First, we ignore spin-orbit coupling and examine the cluster Hamiltonian in the spin-rotation invariant limit. We then include spin-orbit coupling and form cluster states symmetrized with respect to the double group.

A. Cluster states without SOC

Since a single SoD cluster has the same point group symmetry as the $1T$ -TaS₂ crystal lattice (in the absence of the CDW), constructing cluster states is a matter of symmetrizing with respect to D_{3d} . Without spin-orbit coupling there are two degrees of freedom which must be symmetrized: (i) the sites within a cluster and (ii) the orbitals on each site. The orbitals are symmetrized by default and we therefore first consider the sites within a

cluster. We symmetrize these by forming states of definite angular momentum and then construct symmetrized products of site and orbital states.

For the β and γ sites of the cluster, states of definite angular momentum are given by

$$|\beta, l\rangle = \sum_n \frac{e^{i\theta nl}}{\sqrt{6}} |\beta_n\rangle, \quad |\gamma, l\rangle = \sum_n \frac{e^{i\theta nl}}{\sqrt{6}} |\gamma_n\rangle \quad (8)$$

where $l = -2, \dots, 3$ is the angular momentum and $\theta \equiv 2\pi/6$. The central α site coincides with the origin of the cluster and is therefore labeled $l = 0$; the corresponding state is denoted $|\alpha, 0\rangle$. The angular momentum states can be assigned symmetry labels (i.e., irreducible representations) according to their transformation properties. Specifically, the $l = 0$ states have A_1^+ symmetry, the $l = \pm 1$ states have E^- symmetry, and the $l = \pm 2$ states have E^+ symmetry. The symmetry labels of the $l = 3$ states are different for the β and γ sites, which is due to different orientation of the six β and γ sites (see Fig. 3). It is straightforward to determine that $|\beta, 3\rangle$ has A_1^- symmetry and $|\gamma, 3\rangle$ has A_2^- symmetry.

The next step is to include the orbital degrees of freedom and form symmetrized product states of sites and orbitals. In the language of group theory this can be phrased as decomposing the product representation $(3A_1^+ + A_1^- + A_2^- + 2E^+ + 2E^-) \times (A_1^+ + E^+)$, which is the product of site and orbital representations, into irreducible representations of the group D_{3d} . This yields a total of $3 \times 13 = 39$ states, of which five have A_1^+ symmetry, two have A_2^+ symmetry, fourteen have E^+ symmetry, three have A_1^- symmetry, three have A_2^- symmetry, and twelve have E^- symmetry. For example, the five A_1^+

states are

$$|A_1^+(1)\rangle = |\alpha, 0, d_0\rangle, \quad (9)$$

$$|A_1^+(2)\rangle = |\beta, 0, d_0\rangle, \quad (10)$$

$$|A_1^+(3)\rangle = |\gamma, 0, d_0\rangle, \quad (11)$$

which have $l = 0$ and only support on $|d_0\rangle$, and

$$|A_1^+(4)\rangle = (|\beta, 2, d_+\rangle + |\beta, \bar{2}, d_-\rangle)/\sqrt{2}, \quad (12)$$

$$|A_1^+(5)\rangle = (|\gamma, 2, d_+\rangle + |\gamma, \bar{2}, d_-\rangle)/\sqrt{2}, \quad (13)$$

which are states constructed such that the total angular momentum is zero. The remaining states of different symmetry are constructed in the same way and are listed in Appendix D.

As mentioned above, the key upshot of constructing symmetrized cluster states is that such construction block-diagonalizes the cluster Hamiltonian, i.e., the Hamiltonian defined in Sec. II C restricted to a single SoD cluster. All energy levels of a single cluster can thus be resolved by point group symmetry. Note that the energies and eigenstates within a given symmetry block are obtained by diagonalization of the block Hamiltonian; due to multiplicities (e.g. the A_1^+ states have multiplicity five) symmetrization by point does not fully diagonalize the Hamiltonian. Resolving the cluster states (“molecular states”) by symmetry allows for an analysis of the dependence of the cluster energy levels on model parameters, and therefore provides important insight into the nature of the flat band.

The cluster energy levels obtained by diagonalizing the Hamiltonian within each symmetry block is shown in Fig. 4(a)–(c) for three different parameter sets. Specifically, we show three different values of the crystal field splitting Δ . Given a filling of one electron per site, the lowest six cluster levels will be fully filled, and the seventh level will be half filled and can thus be interpreted as the flat band state, i.e., the cluster level which will become the half-filled flat band in the CDW state of weakly coupled clusters. Importantly, we see from Fig. 4(a)–(c) that the nature of the cluster level of interest (indicated in red or green) is different for the three values of the crystal field splitting. In Fig. 4(a) the relevant cluster level (indicated in red) is a twofold degenerate E^+ level, which implies that, in order to obtain a single flat band, spin-orbit coupling is required to split the twofold E^+ level. This corresponds to the scenario discussed in Refs. 15 and 19. In contrast, in Fig. 4(b) the relevant cluster level (red) is a non-degenerate A_1^+ level, in which case a flat band can form in the absence of spin-orbit coupling. This scenario was pointed out in Ref. 18. Upon increasing the value of Δ , we find that a level crossing between the inversion-even A_1^+ level and an inversion-odd A_1^- level can occur, suggesting a further scenario for realizing a flat band in 1T-TaS₂ characterized by an even-odd band inversion. This will be explored further in Sec. IV. Although here we only show the dependence of the cluster energy levels on Δ , in general these energy levels also depend on intra- and interorbital hoppings.

To visualize these orbitals in real space we take the weight obtained from the diagonalization process and project them onto real space orbitals of the hydrogen atom in Fig. 4.(d)-(f), corresponding to the states indicated in panels (a)-(c). Note that for the twofold E^+ states here we show real superposition states.

B. Cluster states in the presence of SOC

When spin-orbit coupling is included the clusters states must be symmetrized with respect to representations of the double group. There are four such representations, which we label $\Gamma_{1/2}^\pm$ and $\Gamma_{3/2}^\pm$ in accordance with total angular momentum $j = 1/2, 3/2$ and which all correspond to twofold degenerate representations (due to crystal and time-reversal symmetry). It is then straightforward to construct spin-orbit coupled symmetrized states from the states constructed above. All states which belong to non-degenerate representations (A_1^\pm and A_2^\pm) fall in the $\Gamma_{1/2}^\pm$ symmetry class, which means that some states previously distinct now have the same symmetry. When coupling the E^\pm states with a spin $S = 1/2$ both $\Gamma_{1/2}^\pm$ and $\Gamma_{3/2}^\pm$ states can be formed, since this amounts to coupling an $L = 1$ and $S = 1/2$ angular momentum to form $j = 1/2, 3/2$. For instance, taking the α states as an example, we form the states

$$|\Gamma_{3/2}^+, 3/2\rangle = |\alpha, 0, d_+, \uparrow\rangle, \quad (14)$$

$$|\Gamma_{3/2}^+, \bar{3}/2\rangle = |\alpha, 0, d_-, \downarrow\rangle. \quad (15)$$

Using this standard prescription we find the following multiplicities: $\Gamma_{1/2}^+$ (14), $\Gamma_{3/2}^+$ (7), $\Gamma_{1/2}^-$ (12) and $\Gamma_{3/2}^-$ (6). In this basis of symmetrized states the spin-orbit coupled cluster Hamiltonian is block-diagonal.

In Fig. 5 we plot the energy spectrum of the spin-orbit coupled cluster states as a function of the orbital detuning Δ for $\theta = \pi/4$. The grey dots denote the electronic ground state occupation in the absence of interaction, which corresponds to 13 filled electronic states. As a result, there is one singly occupied state, which potentially forms the flat band when the SoDs form a lattice structure.

The different panels in the figure depict the spectral flow of these states as a function of the parameter Δ . The even- and odd-parity states are labeled red and green, respectively. As can be seen, the spectral flow also involves an inversion in between even and odd parity states. In the regime between $\Delta < 1.78$ the 7th energy state is the even parity state $\Gamma_{1/2}^+$. Above this threshold it switches to the odd parity $\Gamma_{1/2}^-$. As we will see in the next section such a transition lead to transitions between even and odd flat bands with an intermediate topologically non-trivial band.

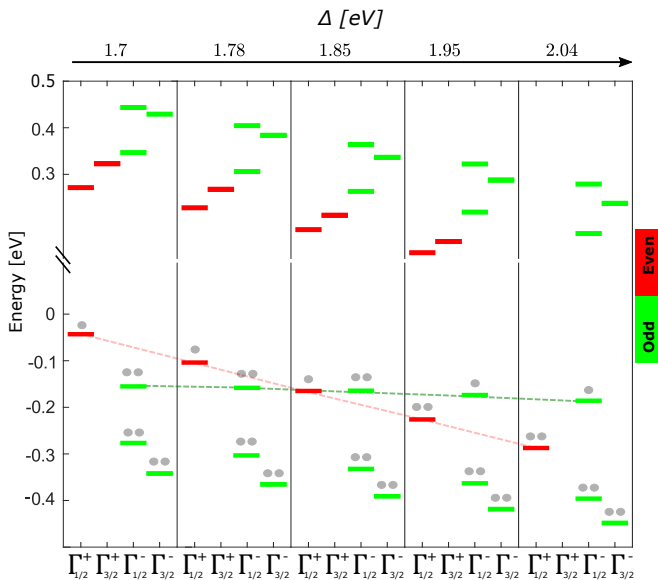


FIG. 5. The spectrum of cluster states for varying values of Δ for $\theta = \pi/4$ [see Eq. (3)]. The color of each state denotes its eigenvalue under inversion. Grey circles indicate level filling.

IV. FLAT BAND INVERSION

The tight binding model we have constructed contains two phenomenological parameters, the orbital splitting Δ and the Wannier orbital spread ξ . To determine realistic values we used an unbiased fit to DFT. In addition to these parameters, we have also introduced the SOC parameters λ_0 and θ , which control the overall and relative strength of diagonal and off-diagonal elements of the SOC matrix, respectively. To gain further insight on the nature of the flat band in 1T-TaS₂, we will now explore the influence of these parameters on the miniband structure by allowing them to vary. (We generally find that the parameter ξ is inconsequential over the range of physically relevant parameters and therefore mainly our focus to the parameters Δ , θ and λ_0 .)

As mentioned in the previous section Sec. III, the flat miniband of interest stems from the seventh cluster state, which is half-filled. We have furthermore demonstrated that the energy levels of the cluster states (when considering single clusters) depends on the orbital bias Δ , and also on the SOC parameters λ_0 and θ . As a result, the structure of the energy level spectrum, and in particular the nature of the flat band state, can vary depending on these three parameters. It also depends on the hopping overlap integrals, but here we focus attention on the dependence on Δ , λ_0 , and θ .

When $\Delta = 0$ and $\lambda_0 = 0$, the seventh cluster state belongs to a fourfold degenerate energy level (including spin), which has E^+ symmetry under D_{3d} . Finite SOC will then split this fourfold level into two twofold energy levels with $\Gamma_{1/2}^+$ and $\Gamma_{3/2}^+$ symmetry, leading to half-filled “band”. Hence, in this scenario, a flat band arises by al-

lowing hopping between the $\Gamma_{1/2}^+$ or $\Gamma_{3/2}^+$ states on neighboring clusters. As alluded to in Sec. III, this is one way to obtain the half-filled flat band in the miniband structure consistent with experiment. In this scenario SOC plays a crucial role. Indeed, this scenario is the one proposed by Ref. [15] and corresponds to the minimal model considered in Ref. [19].

However, we find additional paths to obtaining a single flat band that do not require SOC. For example, by tuning the orbital potential Δ at $\lambda_0 = 0$ above a certain threshold, the seventh cluster state switches its symmetry between the E^+ to A_1^+ irreps. Upon further increasing Δ it switches again to the A_2^- irrep (see Fig. 4). Given that the two latter states belong to a one-dimensional irrep, they provide a different path to obtain a isolated flat band that does not require SOC. Indeed, we find such flat bands in our tight-binding model, even when the SOC coupling is set to zero.

Guided by this microscopic picture we now explore the miniband structure as we tune Δ , λ_0 and θ . We classify three distinct flat bands. Two of these bands, are topologically trivial and classified by the parity of the wave functions at both high symmetry points, Γ and M . The third type of flat band is a topologically non-trivial band with opposite parity at the Γ and M points.

A. The Ising limit ($\theta = 0$)

The limit of $\theta = 0$, although unphysical, is a good starting point to gain intuition. In this limit, the SOC conserves the spin projection along the z axis (S_z) and the tight-binding Hamiltonian (7) becomes block-diagonal, where the two blocks of size 39×39 are identical except for an energy shift due to SOC Eq. (3).

In Fig. 6 we plot the flat band’s dispersion along the trajectory Γ – M – K – Γ , for different values of Δ (panel a) and λ_0 (panel b). The color coding indicates the weight of even/odd cluster states in the Bloch wave-function. Namely, green indicates the weight of odd parity cluster states and red indicates the weight of the even parity ones.

The parity eigenvalues at the high symmetry points, Γ and M can be used to classify the bands into three groups: (i) When the parity at Γ and M is even the band will be referred to as “even” and the Wannier orbital is even under inversion. (ii) When both Γ and M are odd the band will be referred to as “odd” and the Wannier orbital is odd under inversion. (iii) When the parity at Γ and M is opposite the band has a non-trivial \mathbb{Z}_2 topological invariant [28, 29]. In this case a time-reversal invariant Wannier representation of the band is obstructed [30] and thus the orbitals are expected to be extended.

As can be seen in Fig. 6(a) tuning the potential Δ drives a transition between even and odd bands with an intermediate topologically non-trivial band. The cluster state classification of the Γ -point wave function in this

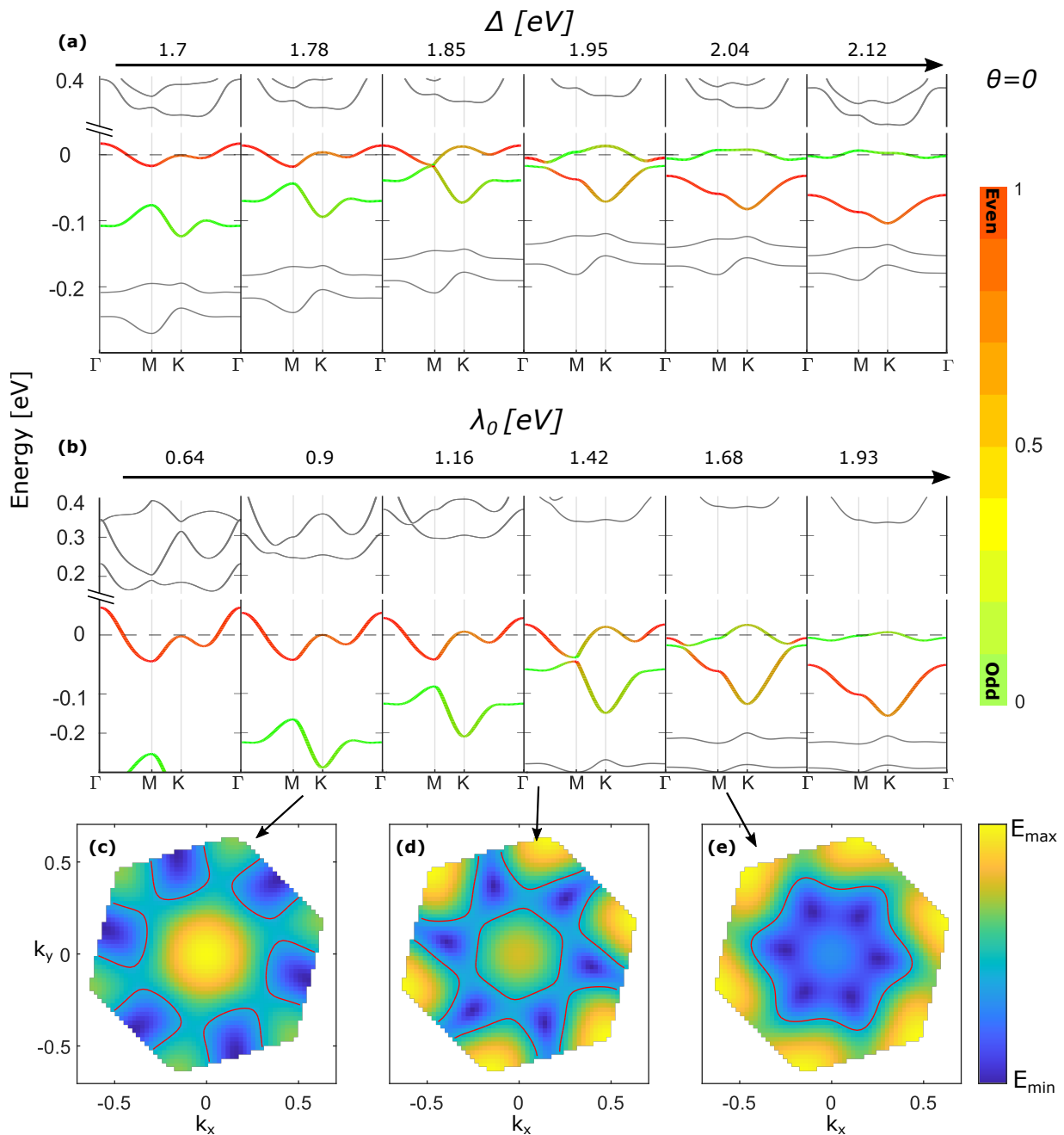


FIG. 6. (a) The dispersion in the mini-Brillouin zone for varying values of Δ , $\lambda_0 = 0.64$ eV and $\theta = 0$. (b) Same for varying λ_0 and $\Delta = 0.13$ eV. The color indicates the relative weight of even and odd orbitals in the Bloch wave function. (c) to (e) are color maps of the dispersion of the flat band at indicated values of λ_0 . The red lines indicate the Fermi surface at half-filling.

case is either A_1^+ or E^+ depending on parameters (See Fig.4). On the other hand, the odd band belongs to the A_2^- irrep.

The same behavior is observed upon increasing the spin-orbit coupling strength λ_0 at constant Δ (panel b). In panels (c)-(e) we plot the band dispersion (and the Fermi surface at half-filling) for three indicated values. Mirror symmetry breaking of the SoD CDW is manifest in the dispersion relations. Namely, they have a “swirling” structure reminiscent of a Plumeria flower.

B. The isotropic case ($\theta = \pi/4$)

When $\theta \neq 0$, the spin projection along z is no longer a good quantum number. In what follows we consider the isotropic limit where $\theta = \pi/4$, which corresponds to the limit where the coordination of sulfur atoms surrounding the tantalum is a perfect octahedron and the d -orbitals form an effective $l = 1$ irrep.

In Fig. 7 we plot the classification of the flat band as

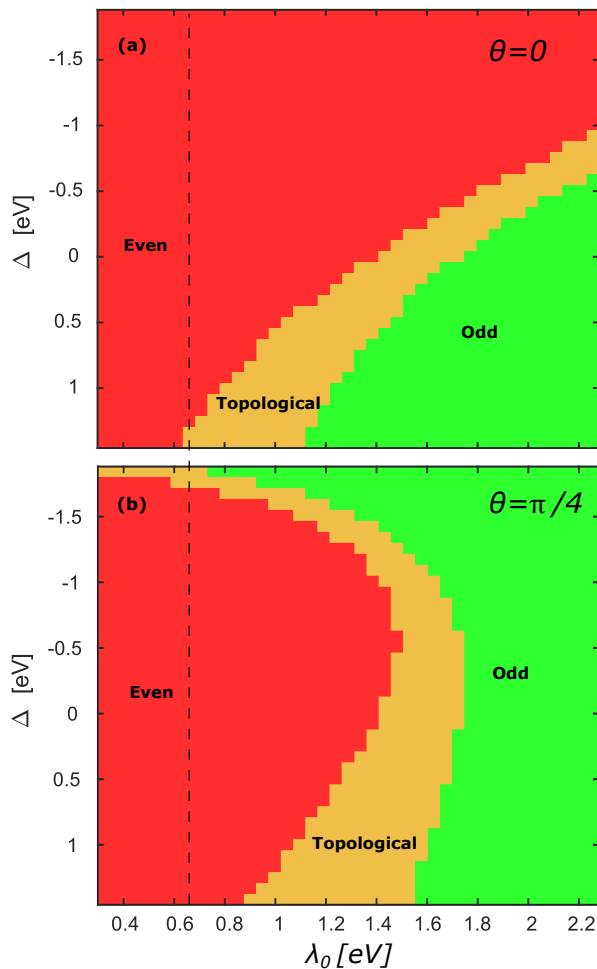


FIG. 7. The phase diagrams of the flat band as a function of Δ , and SOC strength, λ_0 . Red and green indicate bands which are even and odd at both high symmetry points, respectively (see text). The orange area denotes regions where the band has a non-trivial topological index. (a) The phase diagram for $\theta = 0$ and (b) for $\theta = \pi/4$.

a function of λ_0 and Δ . We compare the phase diagram of the Ising case ($\theta = 0$) case (panel a) with the isotropic case ($\theta = \pi/4$) (panel b). As can be seen, the phase space of the topological band is enhanced in the isotropic case. Secondly, the odd parity band is promoted to the $\Delta > 0$ region as well.

As we have mentioned above the existence of inversion symmetry endows the band with a \mathbb{Z}_2 topological index. When the Bloch wave-function has different inversion eigenvalues at the high symmetry points Γ and M the index is 1 and the band is topologically non-trivial [28].

V. DISCUSSION

We have derived a tight-binding model for 1T-TaS₂, which includes the effects of spin-orbit coupling and the star-of-David charge density wave. We found that a sin-

gle half-filled flat band at the Fermi level is a robust feature of this model in the sense that it exists over a wide range of parameters. The flat band can be obtained with or without spin-orbit coupling and may differ in its symmetry properties and even its topological classification. These results affect the low-energy Hamiltonian in the half-filled Mott state in pristine 1T-TaS₂ and also to doped samples, such as 4Hb-TaS₂ [31] and ionic gel gating [32].

First, the off-diagonal elements in the SOC matrix included in our tight-binding model Eq. (3) entail the absence of spin conservation. The authors of Ref. 19 derived an effective low-energy spin-spin Hamiltonian in the Mott state while assuming this symmetry is present. Consequently, they arrived at an XXZ Hamiltonian (up to nearest neighbour couplings)

$$H_{XXZ} = \sum_{\langle ij \rangle} [J_{\perp} (S_i^x S_j^x + S_i^y S_j^y) + J_{ZZ} S_i^z S_j^z]. \quad (16)$$

However, once spin conservation symmetry is absent a more general Hamiltonian is allowed [33]

$$H = H_{XXZ} + \sum_j \sum_{l=1}^3 \left[J_1 (\cos \phi_l \mathcal{T}_{j, \mathbf{a}_l}^{xz} + \sin \phi_l \mathcal{T}_{j, \mathbf{a}_l}^{yz}) + J_2 (\cos 2\phi_l (\mathcal{T}_{j, \mathbf{a}_l}^{xx} - \mathcal{T}_{j, \mathbf{a}_l}^{yy}) + \sin 2\phi_l \mathcal{T}_{j, \mathbf{a}_l}^{xy}) \right], \quad (17)$$

where $\phi_l = \phi_0 + 2\pi l/3$ and $\mathcal{T}_{j, \mathbf{a}_l}^{\alpha\beta} \equiv (S_j^{\alpha} S_{j+\mathbf{a}_l}^{\beta} + S_j^{\beta} S_{j+\mathbf{a}_l}^{\alpha})/2$.

The Hamiltonian Eq. (17) is a generalized version of the Heisenberg-Kitaev [34] model (also known as the $J-K-\Gamma-\Gamma'$ model) on a triangular lattice [33, 35]. The values of the couplings J_1 , J_2 and ϕ_0 can not be determined based on symmetry alone and require a microscopic calculation [36]. It is important to note that a finite angle ϕ_0 is unique to 1T-TaS₂. It reflects the breaking of \mathcal{C}_{2x} by the SoD CDW. The ground state of this model depends strongly on the parameters and may include spin-liquid ground states [33].

As we have seen the topological classification of the flat band can be tuned using the parameters Δ , λ_0 and θ . The existence of a topologically non-trivial flat band in the phase space is interesting for multiple reasons. First, when the topological index is non-trivial there is no local Wannier representation without breaking time-reversal symmetry. Therefore, the fate of the strongly correlated band at half filling is not clear [37–42]. Second, there will be topological edge states running between the flat and remote bands, which may be observed even in the presence of bulk states. Finally, quantum geometrical effects are expected to be strong even in the metallic states. The latter point is especially relevant to samples where the density is doped away from half-filling. This can be obtained by ionic liquid gel gating [32] or naturally occur due to work function differences to adjacent two-dimensional layers, as observed in 4Hb-TaS₂ [31, 43–45].

It is thus interesting to consider the Fermi surface instabilities of the doped flat miniband in 1T-TaS₂ (see panels (c)-(e) of Fig. 6). In this case we may expect spontaneous symmetry breaking states such as ferromagnetism or electronic ferroelectricity [46, 47].

VI. ACKNOWLEDGMENTS

We thank Roser Valenti, Binghai Yan, Natalia Perkins, Assa Aurbach, Amit Kanigel and Anna Keselman for

helpful discussions. J.R. was funded by the Israeli Science Foundation grant No. 3467/21. J.W.F.V. was supported by the National Science Foundation Award No. DMR-2144352.

-
- [1] Joseph G Checkelsky, B Andrei Bernevig, Piers Coleman, Qimiao Si, and Silke Paschen, “Flat bands, strange metals and the kondo effect,” *Nature Reviews Materials*, 1–18 (2024).
- [2] M. E. Zhitomirsky and Hirokazu Tsunetsugu, “Exact low-temperature behavior of a kagomé antiferromagnet at high fields,” *Phys. Rev. B* **70**, 100403 (2004).
- [3] Rafi Bistritzer and Allan H MacDonald, “Moiré bands in twisted double-layer graphene,” *Proceedings of the National Academy of Sciences* **108**, 12233–12237 (2011).
- [4] Päivi Törmä, “Essay: Where can quantum geometry lead us?” *Physical Review Letters* **131**, 240001 (2023).
- [5] Siddharth A Parameswaran, Rahul Roy, and Shivaji L Sondhi, “Fractional quantum hall physics in topological flat bands,” *Comptes Rendus Physique* **14**, 816–839 (2013).
- [6] Emil J Bergholtz and Zhao Liu, “Topological flat band models and fractional chern insulators,” *International Journal of Modern Physics B* **27**, 1330017 (2013).
- [7] Leon Balents, Cory R Dean, Dmitri K Efetov, and Andrea F Young, “Superconductivity and strong correlations in moiré flat bands,” *Nature Physics* **16**, 725–733 (2020).
- [8] NV Smith, SD Kevan, and FJ DiSalvo, “Band structures of the layer compounds 1T-TaS₂ and 2H-TaSe₂ in the presence of commensurate charge-density waves,” *Journal of Physics C: Solid State Physics* **18**, 3175 (1985).
- [9] FJ Di Salvo and S Mahajan, “Charge-density waves and superlattices in the metallic layered transition metal dichalcogenides,” *Advances in Physics* **24**, 117–201 (1975).
- [10] FJ Di Salvo and JE Graebner, “The low temperature electrical properties of 1T-TaS₂,” *Solid State Communications* **23**, 825–828 (1977).
- [11] A. Ribak, I. Silber, C. Baines, K. Chashka, Z. Salman, Y. Dagan, and A. Kanigel, “Gapless excitations in the ground state of 1T-TaS₂,” *Phys. Rev. B* **96**, 195131 (2017).
- [12] K. T. Law and Patrick A Lee, “1T-TaS₂ as a quantum spin liquid,” *Proceedings of the National Academy of Sciences* **114**, 6996–7000 (2017).
- [13] Emma C Regan, Danqing Wang, Chenhao Jin, M Iqbal Bakti Utama, Beini Gao, Xin Wei, Sihan Zhao, Wenyu Zhao, Zuocheng Zhang, Kentaro Yumigeta, *et al.*, “Mott and generalized wigner crystal states in WSe₂/WS₂ moiré superlattices,” *Nature* **579**, 359–363 (2020).
- [14] T Ritschel, H Berger, and J Geck, “Stacking-driven gap formation in layered 1T-TaS₂,” *Physical Review B* **98**, 195134 (2018).
- [15] K. Rossnagel and N. V. Smith, “Spin-orbit coupling in the band structure of reconstructed 1T-TaS₂,” *Phys. Rev. B* **73**, 073106 (2006).
- [16] Xiang-Long Yu, Da-Yong Liu, Ya-Min Quan, Jiansheng Wu, Hai-Qing Lin, Kai Chang, and Liang-Jian Zou, “Electronic correlation effects and orbital density wave in the layered compound 1T-TaS₂,” *Phys. Rev. B* **96**, 125138 (2017).
- [17] Daniel T. Larson, Wei Chen, Steven B. Torrisi, Jennifer Coulter, Shiang Fang, and Efthimios Kaxiras, “Effects of structural distortions on the electronic structure of T-type transition metal dichalcogenides,” *Phys. Rev. B* **102**, 045128 (2020).
- [18] Li Cheng, Xuanyu Long, Xiaobin Chen, Xiaolong Zou, and Zheng Liu, “Understanding the flat band in 1t-tas₂ using a rotated basis,” *Phys. Rev. B* **104**, L241114 (2021).
- [19] Wen-Yu He, Xiao Yan Xu, Gang Chen, Kam Tuen Law, and Patrick A Lee, “Spinon fermi surface in a cluster mott insulator model on a triangular lattice and possible application to 1T-TaS₂,” *Physical review letters* **121**, 046401 (2018).
- [20] Gui-Bin Liu, Wen-Yu Shan, Yugui Yao, Wang Yao, and Di Xiao, “Three-band tight-binding model for monolayers of group-vib transition metal dichalcogenides,” *Phys. Rev. B* **88**, 085433 (2013).
- [21] Sergio C De la Barrera, Michael R Sinko, Devashish P Gopalan, Nikhil Sivadas, Kyle L Seyler, Kenji Watanabe, Takashi Taniguchi, Adam W Tsen, Xiaodong Xu, Di Xiao, *et al.*, “Tuning ising superconductivity with layer and spin-orbit coupling in two-dimensional transition-metal dichalcogenides,” *Nature communications* **9**, 1427 (2018).
- [22] Lei Wang, En-Min Shih, Augusto Ghiotto, Lede Xian, Daniel A Rhodes, Cheng Tan, Martin Claassen, Dante M Kennes, Yusong Bai, Bumho Kim, *et al.*, “Correlated electronic phases in twisted bilayer transition metal dichalcogenides,” *Nature materials*, 1–6 (2020).
- [23] YD Wang, WL Yao, ZM Xin, TT Han, ZG Wang, L Chen, C Cai, Yuan Li, and Y Zhang, “Band insulator to mott insulator transition in 1T-TaS₂,” *Nature communications* **11**, 4215 (2020).
- [24] I. Silber, S. Mathimalar, I. Mangel, A. K. Nayak, O. Green, N. Avraham, H. Beidenkopf, I. Feldman,

- A. Kanigel, A. Klein, M. Goldstein, A. Banerjee, E. Sela, and Y. Dagan, “Two-component nematic superconductivity in 4Hb-TaS₂,” *Nature Communications* **15**, 824 (2024).
- [25] Liguang Ma, Cun Ye, Yijun Yu, Xiu Fang Lu, Xiaohai Niu, Sejoong Kim, Donglai Feng, David Tománek, Young-Woo Son, Xian Hui Chen, *et al.*, “A metallic mosaic phase and the origin of mott-insulating state in 1T-TaS₂,” *Nature communications* **7**, 10956 (2016).
- [26] Gan Liu, Tianyu Qiu, Kuanyu He, Yizhou Liu, Dongjing Lin, Zhen Ma, Zhentao Huang, Wenna Tang, Jie Xu, Kenji Watanabe, *et al.*, “Electrical switching of ferro-rotational order in nanometre-thick 1T-TaS₂ crystals,” *Nature nanotechnology* **18**, 854–860 (2023).
- [27] DI Kochubey, TK Kim, VP Babenko, and Sh K Shaikhutdinov, “Charge density waves in 1t-tas2: an ex-afs study,” *Physica B: Condensed Matter* **252**, 15–20 (1998).
- [28] C. L. Kane and E. J. Mele, “z₂ topological order and the quantum spin hall effect,” *Physical review letters* **95**, 146802 (2005).
- [29] Liang Fu and C. L. Kane, “Topological insulators with inversion symmetry,” *Physical Review B* **76**, 045302 (2007).
- [30] Alexey A Soluyanov and David Vanderbilt, “Wannier representation of Z₂ topological insulators,” *Physical Review B* **83**, 035108 (2011).
- [31] Abhay Kumar Nayak, Aviram Steinbok, Yotam Roet, Jahyun Koo, Gilad Margalit, Irena Feldman, Avior Almoalem, Amit Kanigel, Gregory A Fiete, Binghai Yan, *et al.*, “Evidence of topological boundary modes with topological nodal-point superconductivity,” *Nature physics* **17**, 1413–1419 (2021).
- [32] Yijun Yu, Fangyuan Yang, Xiu Fang Lu, Ya Jun Yan, Yong-Heum Cho, Liguang Ma, Xiaohai Niu, Sejoong Kim, Young-Woo Son, Donglai Feng, *et al.*, “Gate-tunable phase transitions in thin flakes of 1T-TaS₂,” *Nature nanotechnology* **10**, 270–276 (2015).
- [33] P. A. Maksimov, Zhenyue Zhu, Steven R. White, and A. L. Chernyshev, “Anisotropic-exchange magnets on a triangular lattice: Spin waves, accidental degeneracies, and dual spin liquids,” *Phys. Rev. X* **9**, 021017 (2019).
- [34] G. Jackeli and G. Khaliullin, “Mott insulators in the strong spin-orbit coupling limit: From heisenberg to a quantum compass and kitaev models,” *Phys. Rev. Lett.* **102**, 017205 (2009).
- [35] Shi Wang, Zhongyuan Qi, Bin Xi, Wei Wang, Shun-Li Yu, and Jian-Xin Li, “Comprehensive study of the global phase diagram of the J-K-Γ model on a triangular lattice,” *Physical Review B* **103**, 054410 (2021).
- [36] Frank Krüger, Sanjeev Kumar, Jan Zaanen, and Jeroen van den Brink, “Spin-orbital frustrations and anomalous metallic state in iron-pnictide superconductors,” *Physical Review B* **79**, 054504 (2009).
- [37] B. Andrei Bernevig and Shou-Cheng Zhang, “Quantum spin hall effect,” *Phys. Rev. Lett.* **96**, 106802 (2006).
- [38] Titus Neupert, Luiz Santos, Shinsei Ryu, Claudio Chamon, and Christopher Mudry, “Fractional topological liquids with time-reversal symmetry and their lattice realization,” *Phys. Rev. B* **84**, 165107 (2011).
- [39] Titus Neupert, Claudio Chamon, Thomas Iadecola, Luiz H Santos, and Christopher Mudry, “Fractional (chern and topological) insulators,” *Physica Scripta* **2015**, 014005 (2015).
- [40] Valerio Peri, Zhi-Da Song, B Andrei Bernevig, and Sebastian D Huber, “Fragile topology and flat-band superconductivity in the strong-coupling regime,” *Physical review letters* **126**, 027002 (2021).
- [41] Ari M Turner, Erez Berg, and Ady Stern, “Gapping fragile topological bands by interactions,” *Physical review letters* **128**, 056801 (2022).
- [42] Niklas Wagner, Lorenzo Crippa, Adriano Amaricci, Philipp Hansmann, Marcel Klett, EJ König, Thomas Schäfer, D Di Sante, Jennifer Cano, AJ Millis, *et al.*, “Mott insulators with boundary zeros,” *Nature Communications* **14**, 7531 (2023).
- [43] Shiwei Shen, Tian Qin, Jingjing Gao, Chenhaoping Wen, Jinghui Wang, Wei Wang, Jun Li, Xuan Luo, Wenjian Lu, Yuping Sun, and Shichao Yan, “Coexistence of quasi-two-dimensional superconductivity and tunable kondo lattice in a van der Waals superconductor,” *Chinese Physics Letters* **39**, 077401 (2022).
- [44] Lorenzo Crippa, Hyeonhu Bae, Paul Wunderlich, Igor I Mazin, Binghai Yan, Giorgio Sangiovanni, Tim Wehling, and Roser Valentí, “Heavy fermions vs doped mott physics in heterogeneous ta-dichalcogenide bilayers,” *Nature Communications* **15**, 1357 (2024).
- [45] Abhay Kumar Nayak, Aviram Steinbok, Yotam Roet, Jahyun Koo, Irena Feldman, Avior Almoalem, Amit Kanigel, Binghai Yan, Achim Rosch, Nurit Avraham, and Haim Beidenkopf, “First-order quantum phase transition in the hybrid metal–mott insulator transition metal dichalcogenide 4hb-tas 2,” *Proceedings of the National Academy of Sciences* **120** (2023), 10.1073/pnas.2304274120.
- [46] Inti Sodemann, Zheng Zhu, and Liang Fu, “Quantum hall ferroelectrics and nematics in multivalley systems,” *Physical Review X* **7**, 041068 (2017).
- [47] Benjamin E Feldman, Mallika T Randeria, Andrés Gyenis, Fengcheng Wu, Huiwen Ji, Allan H MacDonald, and Ali Yazdani, “Observation of a nematic quantum hall liquid on the surface of bismuth,” *Science* **354**, 316–321 (2016).

Appendix A: Crystallographic and octahedral coordinate systems

In this Appendix we present details of the mapping between the crystallographic and octahedral coordinate systems. As explained in the main text, the crystallographic coordinate system is anchored to the crystallographic plane of the triangular Ta atoms, whereas the octahedral coordinate system is anchored to the octahedrally coordinated S atoms surrounding a Ta atom. This is shown schematically in Fig. 8 (left panel).

We first define the rotation matrix which relates the two coordinate frames. We define three vectors $\hat{n}_{j=1,2,3}$ as

$$\hat{n}_j = -\sin\theta_j\hat{x} + \cos\theta_j\hat{y}, \quad \theta_j = (j-1)\frac{2\pi}{3}, \quad (\text{A1})$$

which are shown in Fig. 8 and are useful to define the unit vectors of the octahedral frame, also shown in Fig. 8 (right panel). Note that for illustration purposes here we have assumed that the S atoms surrounding the Ta

atoms form a perfect octahedron. The unit vectors are then given by

$$\hat{\mathbf{e}}_{\tilde{x},\tilde{y},\tilde{z}} = \sqrt{\frac{2}{3}} \left(\hat{\mathbf{n}}_{1,2,3} + \frac{1}{\sqrt{2}} \hat{\mathbf{z}} \right), \quad (\text{A2})$$

and this triad of unit vectors can be collected in the rotation matrix R as

$$R = (\hat{\mathbf{e}}_{\tilde{x}} \ \hat{\mathbf{e}}_{\tilde{y}} \ \hat{\mathbf{e}}_{\tilde{z}}). \quad (\text{A3})$$

Now R defines a basis transformation relating the crystallographic and octahedral coordinates. In particular, any vector \mathbf{r} can be expanded as

$$\mathbf{r} = x\hat{\mathbf{x}} + y\hat{\mathbf{y}} + z\hat{\mathbf{z}} = \tilde{x}\hat{\mathbf{e}}_{\tilde{x}} + \tilde{y}\hat{\mathbf{e}}_{\tilde{y}} + \tilde{z}\hat{\mathbf{e}}_{\tilde{z}}, \quad (\text{A4})$$

from which it follows that the coordinates are related as

$$\begin{pmatrix} x \\ y \\ z \end{pmatrix} = R \begin{pmatrix} \tilde{x} \\ \tilde{y} \\ \tilde{z} \end{pmatrix}. \quad (\text{A5})$$

Having discussed how the coordinates in the two frames are related, we next consider the relationship between the crystallographic and octahedral basis for the three relevant d -orbitals. In the crystallographic frame—which is the basis used in the main text—the three d states are denoted ($|d_0\rangle, |d_{\pm}\rangle$) and in the octahedral frame the d states are denoted ($|d_{\tilde{y}\tilde{z}}\rangle, |d_{\tilde{z}\tilde{x}}\rangle, |d_{\tilde{x}\tilde{y}}\rangle$) and will be referred to as the octahedral t_{2g} states. The state $|d_0\rangle$ is then expressed in terms of the t_{2g} states as

$$|d_0\rangle = \frac{1}{\sqrt{3}}(|d_{\tilde{y}\tilde{z}}\rangle + |d_{\tilde{z}\tilde{x}}\rangle + |d_{\tilde{x}\tilde{y}}\rangle), \quad (\text{A6})$$

and the two states $|d_{\pm}\rangle$ are given by

$$|d_{\pm}\rangle = \frac{-i}{\sqrt{3}}(|d_{\tilde{y}\tilde{z}}\rangle + e^{\pm 2\pi i/3}|d_{\tilde{z}\tilde{x}}\rangle + e^{\mp 2\pi i/3}|d_{\tilde{x}\tilde{y}}\rangle). \quad (\text{A7})$$

These relations can be collected in a basis transformation matrix U given by

$$U = \frac{1}{\sqrt{3}} \begin{pmatrix} -i & 1 & -i \\ -i\omega & 1 & -i\omega^2 \\ -i\omega^2 & 1 & -i\omega \end{pmatrix}. \quad (\text{A8})$$

One way to obtain this basis transformation matrix is to start from a set of three t_{2g} orbitals ($\tilde{y}\tilde{z}, \tilde{z}\tilde{x}, \tilde{x}\tilde{y}$) expressed in octahedral coordinates, and re-express them in terms of the crystallographic coordinates (x, y, z) using (A5). A subsequent basis transformation U in the space of orbitals then yields the crystallographic orbitals $2z^2 - x^2 - y^2$ (corresponding to the state $|d_0\rangle$) and $i(x \mp iy)^2 \pm \sqrt{2}z(x \pm iy)$ (corresponding to the states $|d_{\pm}\rangle$). It is important to stress that this assumes a perfect octahedral environment of the Ta atoms. In the case of trigonally distorted TaS₆ octahedra the $|d_{\pm}\rangle$ states are some linear combination of the orbitals $i(x \mp iy)^2$ and $\pm z(x \pm iy)$, which have the same symmetry under

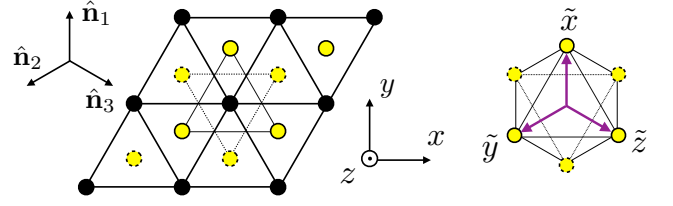


FIG. 8. Relationship between coordinate systems used in this paper. Left: The crystal axes from above x, y , & z relative to the crystal structure. Black dots are Ta atoms while yellow ones are S atoms. The solid vs. dashed border distinguishes between S atoms above and below the plane, respectively. Right: The octahedral coordinate system \tilde{x}, \tilde{y} , & \tilde{z} . Notice that all three have a positive projection on the z axis.

D_{3d} and can therefore mix with coefficients not fixed by symmetry.

We note that this is rather different for $1H$ TMDs with D_{3h} symmetry. The orbitals $i(x \mp iy)^2$ and $\pm z(x \pm iy)$ have distinct symmetry under D_{3h} symmetry and therefore cannot mix. This has consequences for the form of spin-orbital coupling, for instance, as pointed out in the main text and further discussed in Appendix C below.

Appendix B: Crystal lattice symmetries

The symmetries of the crystal lattice play a key role in the analysis presented in the main text. This Appendix discusses further details of the crystal symmetry properties of $1T$ -TaS₂, in particular the representations of the crystal point group in the space of the three d -orbitals.

As mentioned in the main text, pristine $1T$ -TaS₂ has trigonal point group D_{3d} , which is generated by the three-fold rotation C_{3z} , two-fold rotation C_{2x} , and the inversion \mathcal{I} . (Note that the two-fold rotation C_{2x} is broken in the commensurate CDW state.) For reference, the character table for the group D_{3d} is reproduced in Table II. All three states $|d_0\rangle$ and $|d_{\pm}\rangle$ are invariant under inversion. The state $|d_0\rangle$ is furthermore invariant under the threefold and twofold rotations C_{3z} and C_{2x} , and therefore transforms as A_1^+ . The states $|d_{\pm}\rangle$ transform under rotations as

$$C_{3z} : |d_{\pm}\rangle \rightarrow e^{\mp 2\pi i/3} |d_{\pm}\rangle, \quad C_{2x} : |d_{\pm}\rangle \rightarrow |d_{\mp}\rangle, \quad (\text{B1})$$

and thus transform as E^+ . As a result, the matrix representations of the rotation symmetries in the space of orbitals are given by

$$C_{3z} = \begin{pmatrix} \omega^2 & 0 & 0 \\ 0 & 1 & 0 \\ 0 & 0 & \omega \end{pmatrix}, \quad C_{2x} = \begin{pmatrix} 0 & 0 & 1 \\ 0 & 1 & 0 \\ 1 & 0 & 0 \end{pmatrix}. \quad (\text{B2})$$

Note that the matrix representation of the inversion \mathcal{I} is equal to the identity. In addition D_{3d} point group symmetry, both the normal state and the CDW state of

TABLE II. Character table of D_{3d} point group

D_{3d}	1	C_{3z}	C_{2x}	\mathcal{I}	$\mathcal{I}C_{3z}$	\mathcal{M}_{2x}
A_1^\pm	1	1	1	± 1	± 1	± 1
A_2^\pm	1	1	-1	± 1	± 1	∓ 1
E^\pm	2	-1	0	± 2	∓ 1	0

$1T$ -TaS₂ have time-reversal symmetry \mathcal{T} . Time-reversal leaves $|d_0\rangle$ invariant but acts on $|d_\pm\rangle$ as

$$\mathcal{T} : |d_\pm\rangle \rightarrow -|d_\mp\rangle. \quad (\text{B3})$$

These symmetries can be used to determine the form of Hamiltonian in Eq. (1), in particular the allowed hoppings. Consider the nearest neighbor hopping matrix in the direction of \mathbf{a}_1 (see Fig. 1), which we denote T_1 . Inversion symmetry and the twofold rotation C_{2x} impose the constraints $T_1 = T_1^\dagger$ and $C_{2x}T_1C_{2x}^\dagger = T_1$, respectively. Time-reversal symmetry gives an additional constraint, leading to the most general form of the hopping matrix given by

$$T_1 = \begin{pmatrix} t_2 & it_3 & t_4 \\ -it_3 & t_1 & -it_3 \\ t_4 & it_3 & t_2 \end{pmatrix}. \quad (\text{B4})$$

Here $t_{1,2,3,4}$ are the four independent real hoppings parameters used to parametrize the Hamiltonian Eq. (1). The hopping matrices $T_{2,3}$ corresponding to the bond directions $\mathbf{a}_{2,3}$ are obtained by applying the threefold rotation C_{3z} .

It is straightforward to determine the form of the symmetry operators in the octahedral basis. Making use of the basis transformation matrix U given by (A8), we find

$$\tilde{C}_{3z} = UC_{3z}U^\dagger = \begin{pmatrix} 0 & 1 & 0 \\ 0 & 0 & 1 \\ 1 & 0 & 0 \end{pmatrix}, \quad (\text{B5})$$

$$\tilde{C}_{2x} = UC_{2x}U^\dagger = \begin{pmatrix} 1 & 0 & 0 \\ 0 & 0 & 1 \\ 0 & 1 & 0 \end{pmatrix}, \quad (\text{B6})$$

which is consistent with what would be expected for three t_{2g} orbitals with $(\tilde{y}\tilde{z}, \tilde{z}\tilde{x}, \tilde{x}\tilde{y})$ symmetry.

The hopping matrix T_1 may also be expressed in terms of the octahedral basis. Symmetry considerations dictate that the hoppings matrix in the octahedral basis, denoted \tilde{T}_1 , takes the form

$$\tilde{T}_1 = \begin{pmatrix} t_a & t_c & t_c \\ t_c & t_b & t_d \\ t_c & t_d & t_b \end{pmatrix}, \quad (\text{B7})$$

where $t_{a,b,c,d}$ are four hopping parameters in the octahedral basis. Setting this expression for \tilde{T}_1 equal to UT_1U^\dagger , we obtain a relationship between the two different hop-

ping parametrizations. Specifically, we find

$$\begin{pmatrix} t_a \\ t_d \\ t_c \end{pmatrix} = \frac{1}{3} \begin{pmatrix} 1 & 2 & 4 & 2 \\ 1 & 2 & -2 & -1 \\ 1 & -1 & 1 & -1 \\ 1 & -1 & -2 & 2 \end{pmatrix} \begin{pmatrix} t_1 \\ t_2 \\ t_3 \\ t_4 \end{pmatrix}. \quad (\text{B8})$$

Note that the matrix which relates the two sets of hopping parameters is its own inverse.

Appendix C: Spin-orbit coupling in D_{3d} and D_{3h}

This Appendix elaborates on the discussion of spin-orbit coupling in TMD materials (Sec. II B), in particular the differences between the D_{3d} and D_{3h} structures.

The explicit form of the orbital angular momentum matrices $\mathbf{L} = (L_x, L_y, L_z)$ used in Eq. (3) is given by

$$L_z = \begin{pmatrix} 1 & 0 & 0 \\ 0 & 0 & 0 \\ 0 & 0 & -1 \end{pmatrix}, \quad L_+ = L_-^\dagger = \begin{pmatrix} 0 & \sqrt{2} & 0 \\ 0 & 0 & \sqrt{2} \\ 0 & 0 & 0 \end{pmatrix} \quad (\text{C1})$$

where we used the basis ($|d_+\rangle, |d_0\rangle, |d_-\rangle$) for the orbitals. Note that in this basis the orbital angular momentum matrices take the standard form of an $S = 1$ spin angular momentum and have the expected transformation properties under all symmetries. As mentioned in the main text, the parameter θ introduced in Eq. (3) is related to the orbital content of the three states valence and conduction states ($|d_+\rangle, |d_0\rangle, |d_-\rangle$). In particular, in the Ising limit ($\theta = 0$) these three states exactly correspond to the orbitals $i(x \mp iy)^2$ (d_\pm) and $2z^2 - x^2 - y^2$ (d_0), here expressed in crystallographic coordinates.

The Ising limit is therefore applicable to the $1H$ structures with point group D_{3h} , since D_{3h} symmetry forbids mixing between the $i(x \mp iy)^2$ orbitals and the $\pm z(x \pm iy)$ orbitals (see also Appendix A). Indeed, the $i(x \mp iy)^2$ orbitals are even under the horizontal mirror reflection σ_h , whereas the $\pm z(x \pm iy)$ orbitals are odd. As was noted previously in Ref. 20, when projecting the isotropic atomic spin-orbit coupling Hamiltonian of the full five $L = 2$ d -states into the subspace of the three orbitals given by $d_{x^2-y^2}$, d_{xy} , and d_{z^2} , only the Ising term survives.

In the $1T$ structures with point group D_{3d} the local environment of the Ta atoms is very different. Indeed, rather than a triangular prism, as in the $1H$ structures, the S atoms form a (distorted) octahedron. This implies that in general the $i(x \mp iy)^2$ and $\pm z(x \pm iy)$ orbitals will mix, since they have the same symmetry under D_{3d} . Now, the spin-flip terms in H_{SO} need not vanish, giving rise to the more general form of Eq. (3). Since the degree of mixing is material-specific, so is the parameter θ .

The orbital angular momentum matrices can also be expressed in the octahedral basis. Denoting the \tilde{z} component as $\tilde{L}_{\tilde{z}}$, one has

$$\tilde{L}_{\tilde{z}} = U\hat{e}_{\tilde{z}} \cdot \mathbf{L}U^\dagger, \quad (\text{C2})$$

where U was defined in Eq. (A8). Similar expressions hold for the \tilde{x} and \tilde{y} components. In the octahedral basis the orbital angular momentum matrices have the familiar form

$$\tilde{L}_{\tilde{z}} = \begin{pmatrix} 0 & -i & 0 \\ i & 0 & 0 \\ 0 & 0 & 0 \end{pmatrix}, \tilde{L}_{\tilde{x}} = \begin{pmatrix} 0 & 0 & 0 \\ 0 & 0 & -i \\ 0 & i & 0 \end{pmatrix}, \tilde{L}_{\tilde{y}} = \begin{pmatrix} 0 & 0 & i \\ 0 & 0 & 0 \\ -i & 0 & 0 \end{pmatrix}, \quad (\text{C3})$$

which emphasizes the equivalence of the octahedral axes.

Appendix D: Construction of cluster states

In Section III of the main text we have described the construction of symmetrized cluster states, states which transform irreducibly under the crystal symmetry group (D_{3d}) of a single cluster. We gave explicit expressions for the states with A_1^+ symmetry. Here we provide explicit expressions for the remaining states.

The two states with A_2^+ symmetry are given by

$$|A_2^+(1)\rangle = (|\beta, 2, d_+\rangle - |\beta, \bar{2}, d_-\rangle)/\sqrt{2}, \quad (\text{D1})$$

$$|A_2^+(2)\rangle = (|\gamma, 2, d_+\rangle - |\gamma, \bar{2}, d_-\rangle)/\sqrt{2}. \quad (\text{D2})$$

The three states with A_1^- symmetry are given by

$$|A_1^-(1)\rangle = |\beta, 3, d_0\rangle, \quad (\text{D3})$$

$$|A_1^-(2)\rangle = (|\beta, 1, d_-\rangle + |\beta, \bar{1}, d_+\rangle)/\sqrt{2}, \quad (\text{D4})$$

$$|A_1^-(3)\rangle = (|\gamma, 1, d_-\rangle - |\gamma, \bar{1}, d_+\rangle)/\sqrt{2}. \quad (\text{D5})$$

The three states with A_2^- symmetry are given by

$$|A_2^-(1)\rangle = |\gamma, 3, d_0\rangle, \quad (\text{D6})$$

$$|A_2^-(2)\rangle = (|\beta, 1, d_-\rangle - |\beta, \bar{1}, d_+\rangle)/\sqrt{2}, \quad (\text{D7})$$

$$|A_2^-(3)\rangle = (|\gamma, 1, d_-\rangle + |\gamma, \bar{1}, d_+\rangle)/\sqrt{2}. \quad (\text{D8})$$

There are fourteen doublets with E^+ symmetry. Here we choose a basis for this doublet for which the threefold rotation is diagonal and only list one of the partners; the other may be obtained by applying the C_{2x} rotation. The seven states with E^+ symmetry are then

$$|E^+(1)\rangle = |\alpha, 0, d_+\rangle, \quad (\text{D9})$$

$$|E^+(2)\rangle = |\beta, \bar{2}, d_0\rangle, \quad (\text{D10})$$

$$|E^+(3)\rangle = |\gamma, \bar{2}, d_0\rangle, \quad (\text{D11})$$

$$|E^+(4)\rangle = |\beta, 0, d_+\rangle, \quad (\text{D12})$$

$$|E^+(5)\rangle = |\gamma, 0, d_+\rangle, \quad (\text{D13})$$

$$|E^+(6)\rangle = |\beta, 2, d_-\rangle, \quad (\text{D14})$$

$$|E^+(7)\rangle = |\gamma, 2, d_-\rangle. \quad (\text{D15})$$

Similarly, there are twelve doublets with E^- symmetry. Listing only one of the two partners, we have

$$|E^-(1)\rangle = |\beta, 1, d_0\rangle, \quad (\text{D16})$$

$$|E^-(2)\rangle = |\gamma, 1, d_0\rangle, \quad (\text{D17})$$

$$|E^-(3)\rangle = |\beta, 3, d_+\rangle, \quad (\text{D18})$$

$$|E^-(4)\rangle = |\gamma, 3, d_+\rangle, \quad (\text{D19})$$

$$|E^-(5)\rangle = |\beta, \bar{1}, d_-\rangle, \quad (\text{D20})$$

$$|E^-(6)\rangle = |\gamma, \bar{1}, d_-\rangle. \quad (\text{D21})$$